applied sciences

Article

Anomalous Beam Transport through Gabor (Plasma) Lens Prototype

Toby Nonnenmacher [1,*], Titus-Stefan Dascalu [1,*], Robert Bingham [2,3], Chung Lim Cheung [1], Hin-Tung Lau [1], Ken Long [3,4] and Jürgen Pozimski [3,4] and Colin Whyte [2]

[1] Department of Physics, Imperial College London, Exhibition Road, London SW7 2AZ, UK; chung.cheung14@imperial.ac.uk (C.L.C.); h.lau17@imperial.ac.uk (H.-T.L.)
[2] Department of Physics, SUPA, University of Strathclyde, 16 Richmond Street, Glasgow G4 0NG, UK; bob.bingham@stfc.ac.uk (R.B.); colin.whyte@strath.ac.uk (C.W.)
[3] STFC Rutherford Appleton Laboratory, Harwell Oxford, Didcot OX11 0QX, UK; k.long@imperial.ac.uk (K.L.); j.pozimski@imperial.ac.uk (J.P.)
[4] John Adams Institute for Accelerator Science, Imperial College London, London SW7 2AZ, UK
* Correspondence: toby.nonnenmacher14@imperial.ac.uk (T.N.); t.dascalu19@imperial.ac.uk (T.-S.D.)

Abstract: An electron plasma lens is a cost-effective, compact, strong-focusing element that can ensure efficient capture of low-energy proton and ion beams from laser-driven sources. A Gabor lens prototype was built for high electron density operation at Imperial College London. The parameters of the stable operation regime of the lens and its performance during a beam test with 1.4 MeV protons are reported here. Narrow pencil beams were imaged on a scintillator screen 67 cm downstream of the lens. The lens converted the pencil beams into rings that show position-dependent shape and intensity modulation that are dependent on the settings of the lens. Characterisation of the focusing effect suggests that the plasma column exhibited an off-axis rotation similar to the $m = 1$ diocotron instability. The association of the instability with the cause of the rings was investigated using particle tracking simulations.

Keywords: plasma trap; space-charge lens; beam transport; instability; proton therapy

check for updates

Citation: Nonnenmacher, T.; Dascalu, T.S.; Bingham, R.; Cheung, C.L.; Lau, H.T.; Long, K.; Pozimski, J.; Whyte, C. Anomalous Beam Transport through Gabor (Plasma) Lens Prototype. *Appl. Sci.* **2021**, *11*, 4357. https://doi.org/10.3390/app11104357

Academic Editor: Paolo Branchini

Received: 13 April 2021
Accepted: 4 May 2021
Published: 11 May 2021

1. Introduction

One of the principal challenges that must be addressed to deliver high-flux pulsed proton or positive-ion beams for many applications is the efficient capture of the ions ejected from the source. A typical source produces protons with kinetic energies of approximately 60 keV [1–3] and ions with kinetic energies typically below 120 keV [4,5]. At this low energy the mutual repulsion of the ions causes the beam to diverge rapidly. Capturing a large fraction of this divergent flux therefore requires a focusing element of short focal length. Proton- and ion-capture systems in use today employ magnetic, electrostatic, or radio frequency quadrupoles, or solenoid magnets to capture and focus the beam [2,6–8].

Laser-driven proton and ion sources are disruptive technologies that offer enormous potential to serve future high-flux, pulsed beam facilities [9–16]. Possible applications include proton- and ion-beam production for research, particle-beam therapy, radio-nuclide production, and ion implantation. Recent measurements have demonstrated the laser-driven production of large ion fluxes at kinetic energies in excess of 10 MeV [17–20]. The further development of present technologies and the introduction of novel techniques [21,22] makes it conceivable that significantly higher ion energies will be produced in the future [13,23,24]. By capturing the laser-driven ions at energies two orders of magnitude greater than those pertaining to conventional sources, it will be possible to evade the current space-charge limit on the instantaneous proton and ion flux that can be delivered. While in some situations the high divergence of laser-driven ion beams can be reduced [25,26], for the tape-drive targets proposed for medical beams [16,20] it necessary to capture the beam using a strong-focusing element as close to the ion-production point as possible.

An attractive approach to providing the strong-focusing element required to capture the low-energy (∼15 MeV) ion flux produced in the laser-target interaction is to exploit the strong focusing forces that can be provided by a cloud of electrons trapped within a cylindrical volume by crossed electric and magnetic fields. Such an electron-plasma lens was initially proposed by Gabor in 1947 [27]. The use of electron-plasma lenses of the Gabor type to capture and focus proton and ion beams has been studied by a number of authors [28–34]. Such a lens has the potential to decrease the magnetic field required in the first focusing element by a factor of more than 40 compared with that required for a conventional beam-capture solenoid of the same focusing strength [35]. Consider, for example, a 25 MeV proton beam. A magnetic field strength of 0.06 T is required to achieve a focal length of 1 m using a Gabor lens with an anode length of 0.3 m. To achieve the same focal length using a solenoid requires a field of 2.6 T. Such strong focusing is particularly important when beams are produced with a large divergence angle [14]. The Gabor lens is therefore the ideal focusing element by which to capture a laser-accelerated proton or ion beam. Its compactness and relatively low price are key if it is to be exploited in particle-beam therapy facilities. Furthermore, it has been shown in simulation that a Gabor-lens-based system is capable of capturing laser-generated proton beams at energies as high as 250 MeV, the energy required to serve a proton-beam therapy facility [13].

Following the initial proposal by Gabor, several groups have reported stable operation of a space-charge lens under a variety of electrode and magnetic field configurations [28–30,36,37]. Experiments with ion beams confirmed the focusing capability of the Gabor lens and observed emittance growth [30,34,38]. The mechanism for electron production and the inhomogeneity in the electron density within the lens were believed to cause the observed growth in emittance [38].

The focusing strength of a Gabor lens is determined by the electron density. The theoretical maximum electron density is related to the electric and magnetic field strength [13]. Careful design of the field configuration allowed certain lenses to operate at electron densities of 61% of the theoretical maximum [35]. At high pressure, the electrons are lost due to the radial expansion of the plasma driven by collisions with neutral atoms. At low pressure, this radial transport can be caused by small azimuthal asymmetries in the applied electric or magnetic fields [37]. Further work was directed towards the design of an electrostatic lens for the space-charge-compensated transport of a high intensity heavy ion beam [39]. In this case, the absence of emittance growth due to the lens was reported [39].

Advances in simulation and finite-element analysis have been exploited to calculate the expected focusing strength of a space-charge lens and to study the resulting phase-space transformation on a beam passing through the lens. Good agreement between experimental results and beam-transport simulations [34,35] suggest that plasma instabilities are a likely cause of beam aberrations. Experimental observations and numerical results [40] have confirmed that the confined plasma is vulnerable to the diocotron instability [41]. Further studies are required to characterise the configurations under which a Gabor space-charge lens operates in a stable regime.

Plasma-lens focusing for electron beams is being developed by the CERN Linear Electron Accelerator for Research (CLEAR) collaboration [42]. Evidence of aberrations in the CLEAR lens due to radial non-uniformity of the plasma temperature has been observed [43,44]. Previous work at the Stanford Linear Accelerator Center (SLAC) demonstrated the plasma-lens focusing of 28.5 GeV electron [45] and positron [46] beams. Numerical simulations were able to describe the observed non-linear focusing force in this experiment [47]. Discharge-capillary active plasma lenses were also investigated as compact devices for focusing 100 MeV-level electron beams produced by a gas-jet-based laser-plasma accelerator. Both weak and strong chromatic effects [48] were observed with the potential to cause emittance degradation [49]. Research at SLAC seeks to demonstrate the use of such a plasma lens for staging in plasma wakefield acceleration or in radially-symmetric final focusing for linear colliders [50]. As compact and tunable devices, active plasma lenses [51,52] are a promising solution for the extraction and transport of the witness bunch while removing the driver without loss of beam quality [53–55]. Finally, electron plasmas were studied in multicell traps [56,57] to develop methods by which the number of accumulated positrons could be increased compared to the present limits coming from the requirement for long-term confinement.

In this paper we report the performance of a Gabor lens prototype constructed at Imperial College London. The lens was exposed to 1.4 MeV protons at the Surrey Proton Beam Centre [58]. The effect on the beam is presented and compared to the results of a simulation of the impact of plasma instabilities on the focusing forces produced by the lens.

2. The Gabor Lens

A schematic of the prototype Gabor lens is shown in Figure 1. The total length of the lens, from end flange to end flange, was 540 mm. The central anode was formed of a copper cylinder with an inner diameter of 85.7 mm and a length of 444 mm. The copper cylinder was 1.6 mm thick and had four rows of four 10 mm diameter holes forming lines along the axis of the cylinder spaced by 90° so that the volume inside the anode would be evacuated efficiently. Two ceramic isolating spacers were used to maintain the position of the central high-voltage electrode and to electrically isolate it from the vacuum tube. A 15 mm copper high-voltage (HV) connector was soldered to the central electrode to provide a socket for the high-voltage feed-through designed for voltages up to 60–65 kV.

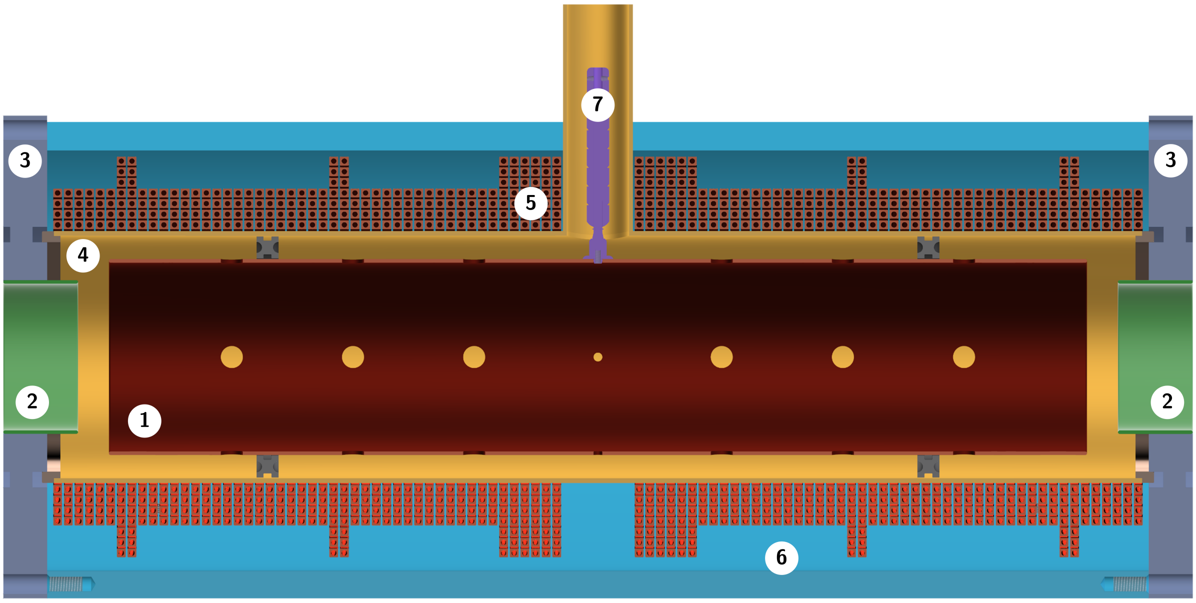

Figure 1. Internal structure of the IC Gabor lens viewed in longitudinal cross-section. The main components are: 1-central anode, 2-end electrodes, 3-end flanges, 4-vacuum tube, 5-pancake coils, 6-outer tube, 7-high-voltage feed-through.

The two end electrodes were formed of two copper cylinders with a length of 34 mm, an inner diameter of 66.7 mm, and a wall thickness of 1.6 mm. The ends of the cylinders were manufactured with rounded edges to reduce the likelihood of sparking, with a minimum gap of 16.8 mm to the high-voltage anode. The end electrodes were press fitted into the mild steed end flanges. The outer tube and end flanges were connected to ground.

The configuration of the pancake coils is shown in Figure 1. The input and output tails of the coils exited through the 50 mm gap in the outer tube of the lens. A water cooled copper conductor was used with a square cross-sectional area of 10.87 mm^2. The base configuration of the coil included four windings. The number of windings was locally increased to seven at specific positions to generate a more uniform magnetic field. A maximum magnetic field of approximately 55 mT was achieved at 45 A.

A power supply (Glassman LP 60–46) was used to regulate the current that flows through the coils. Typical values for the current were in the range of 14 A to 30 A. The voltage for the central electrode was provided by a high-voltage supply of the Glassman Series FR type with typical values of between 8 kV and 20 kV.

The pumping system was comprised of a roughing pump (Edwards 5) and a turbo molecular pump (Leybold Turbovac 151) with a pressure gauge (Leybold Penninvac PTR 90 N) and a pressure-gauge monitor (Leybold Graphix One). The lowest pressure achieved was 3×10^{-7} mbar, with pressures of up to 3×10^{-5} mbar when a non-neutral plasma was established inside the lens. Settings of HV and current that produced a stable plasma could be distinguished clearly from those which gave rise to an unstable plasma at low pressure ($\sim 10^{-7}$ mbar). For higher pressures, this distinction was more difficult to observe.

Plasma in the lens was produced by increasing the high voltage applied to the anode and the current in the magnetic coils. A significant increase in pressure was observed when a stable plasma was first established in the lens. Simulation of the plasma discharge within the lens indicated that a high electron density, $\sim 5 \times 10^{-7}$ cm^{-3}, was produced.

3. Plasma Characterisation

The operation of the lens was tested over the range of available anode voltages and coil currents to identify the regime for which a stable plasma could be produced. Measurements of the plasma in the lens were made using the Medusa voltage sensor shown in Figure 2. The sensor detects the current of ions and electrons discharged by the lens and was composed of 16 equal segments with a total area of 122.5 mm^2. The detector segments were connected either in concentric circles or in a sector arrangement, with four segments combined and fed into one channel of an oscilloscope. The Medusa detector was used to characterise the range of high voltage and current settings which would produce a stable plasma within the lens. A schematic diagram of the experimental setup for these primary studies is given in Figure 3. For a constant current through the coils of the lens, producing a constant magnetic field, the high voltage was increased from zero until plasma was produced in the lens. The presence of a stable plasma in the lens was indicated by a steady voltage read from the Medusa detector. The high voltage was then increased further, until instability in the plasma, characterised by sparking, was observed as an extreme variation in the output voltage reading.

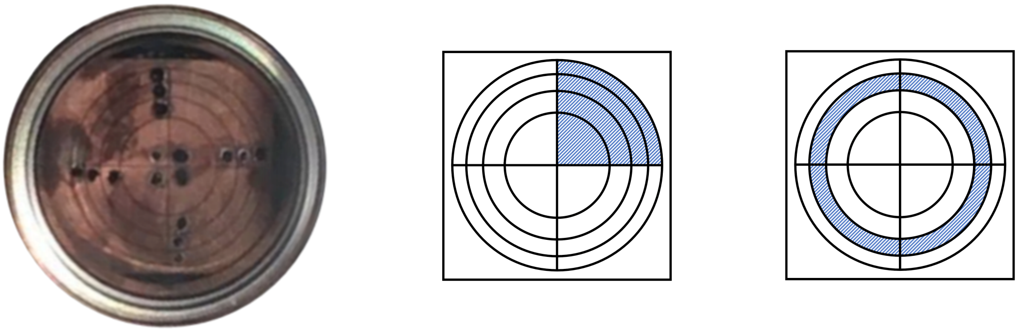

Figure 2. The segmented detector used for measuring the current of electrons and ions exiting the Gabor Lens. The detector is divided in to 16 sections of equal area which were combined in sector (middle) or concentric circle (right) arrangements.

Figure 4 shows the amplitude responses observed in the Medusa detector that are typical of three modes of operation:

- Plasma off: high voltage and current through coils. below the threshold for plasma to be produced;
- Stable plasma: plasma produced with high voltage below 25 kV and current below 27 A; and
- Unstable plasma: plasma produced with higher magnetic field causing considerable sparking and therefore large variations in the output amplitude.

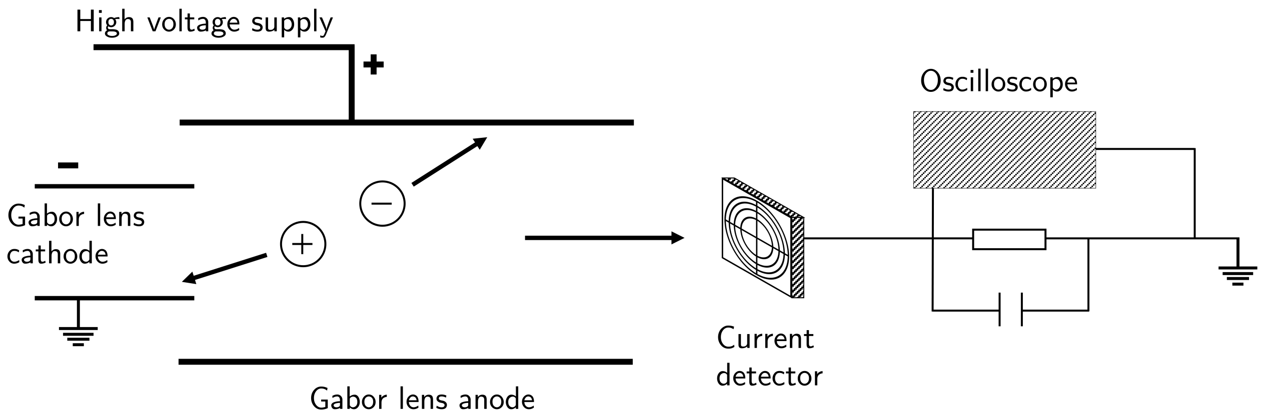

Figure 3. Schematic of the Gabor lens, current detector, and oscilloscope. The high voltage supply maintains the drop across the electrodes. Expelled ions hit the detector, and the current signal is converted to a voltage output signal in the oscilloscope.

The mean and standard deviation of the Medusa voltage measurement of the different plasma regions are shown in Table 1. The mean increases slightly when the plasma is switched on, while the standard deviation remains largely unchanged. As the current applied through the coils becomes large, and the unstable region is reached, the mean and standard deviation rose and a large amount of noise was observed. This is shown in Figure 4, where the level of noise is similar with the plasma off and the plasma on. The noise increases appreciably only when the unstable region is reached. The frequency spectrum of the voltage signal was studied in each of the three modes of operation. In the unstable region, the low-frequency noise is increased significantly while the high-frequency noise remains largely unchanged. The characterisation of the operating regimes described in this section was used to verify that the lens produced a stable plasma during the beam test.

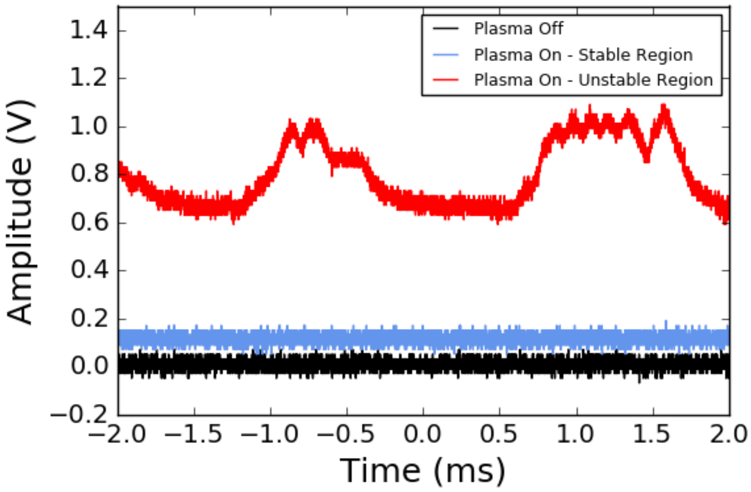

Figure 4. Amplitude of signal from the Medusa detector in three regions: plasma off, plasma on, and plasma on in unstable region. The time range is given 0.0004 s, and the time resolution of the measurement is 4×10^{-7} s. The voltage range is 0.5 V with a resolution of 0.01 V.

Table 1. Mean and Standard Deviation values for Plasma Off, On, and Unstable regions shown in Figure 4.

	Mean (V)	Standard Deviation (V)
Plasma Off	0.008	0.019
Plasma On	0.114	0.020
Plasma Unstable	0.797	0.133

4. Beam Test Setup

The prototype Gabor lens was exposed to proton beams with a kinetic energy of 1.4 MeV at the Ion Beam Facility at the University of Surrey [58] in October 2017. Schematic diagrams of the two setups used in the beam tests are shown in Figure 5. The proton beam entered the lens through a section of evacuated beam pipe. The length of the drift on the first day of data taking was approximately 380 mm (Setup 1 in Figure 5). On the second day the length of the drift was extended to approximately 680 mm to exploit the divergence of the beam to illuminate a larger area at the front face of the lens (Setup 2 in Figure 5).

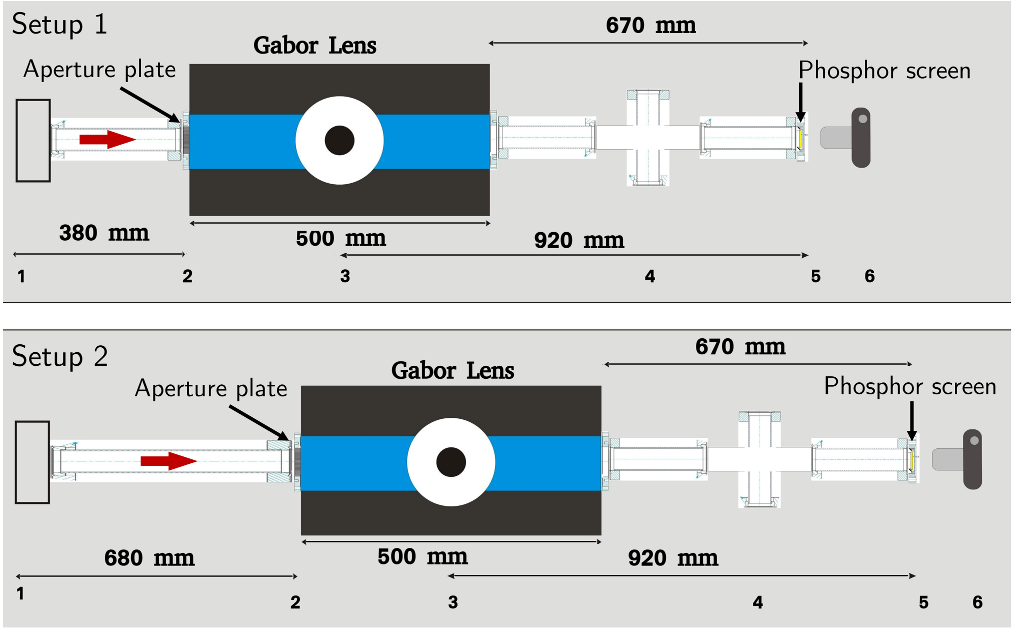

Figure 5. Schematics of the day 1 beam test setup, Setup 1 (**top**) and the day 2 beam test setup, Setup 2 (**bottom**). The setup includes the Gabor lens, aperture, and beam pipes.

Narrow "beamlets" were created using an aperture plate placed at the entrance to the lens (see Figure 6). The holes in the aperture plate were 2 mm in diameter and arranged in a pattern designed to minimise the overlap of the outgoing beamlets under a focusing force that is rotationally symmetric about the beam axis.

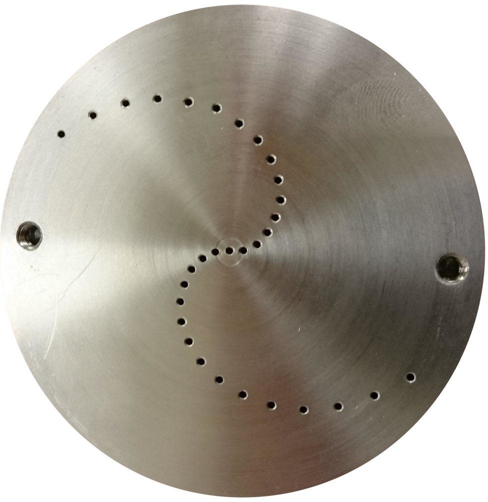

Figure 6. Photograph of the aperture placed in the beamline upstream of the Gabor lens. 30 holes of 2 mm width are drilled in a symmetrical pattern around one further hole on the axis. The surrounding holes are pitched at an angle of 20°.

A further section of evacuated beam pipe of length 670 mm was attached to the downstream flange of the prototype lens. A phosphor screen was installed on the downstream flange as indicated in Figure 5. The phosphor screen used was a P43 phosphor surface on an aluminised pyrex substrate with an effective area of diameter 44.9 mm and a thickness of 10–15 µm as shown in figure 7. Photographs of the image of the beam on the phosphor screen were acquired with a DSLR camera using an exposure long compared to the beam spill.

Figure 7. Photograph and schematic of the phosphor screen used for imaging the beam. The screen was composed of a P43 phosphor surface on a substrate of aluminised pyrex, and the scale and resolution of the screen are shown on the schematic.

5. Characterisation of Lens Performance

The lens was set up on the beam line and stable operation of the lens was established as described in Section 3. The voltage-current characteristics of the lens measured using the Medusa detector with the lens on the beam line are compared with those measured at Imperial in Figure 8. The two sets of measurements show similar features indicating that the lens was operating in a similar manner to the operation in the lab at Imperial. Figure 8 was used to determine that the lens was operating in the stable regime.

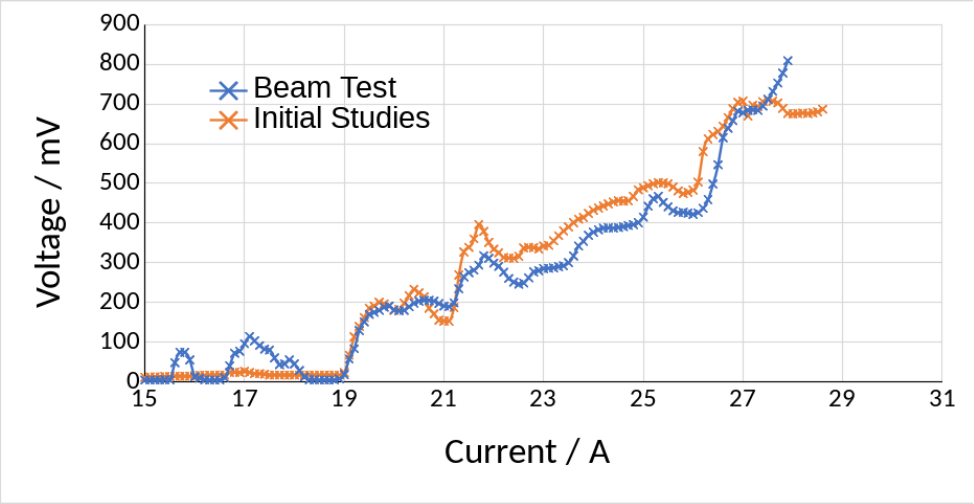

Figure 8. Voltage-current characteristic of the Gabor lens measured with the lens on the beam line (blue crosses) compared to measurements in the laboratory at Imperial (orange crosses). During the beam test the gas pressure in the lens was 10% higher than the pressure at which the lens operated in the laboratory.

Images of beam impinging on the phosphor screen were taken with the lens turned off in both the Setup 1 and Setup 2 configurations (see Figure 9). Distinct "spots" were visible that corresponded to the beamlets produced by the holes in the aperture plate. The longer drift introduced in the Setup 2 configuration resulted in a larger number of beamlets being observed at lower magnification than in the Setup 1 configuration. The central axis of the lens passed through the centre of the second beamlet from the right in both Setup 1 and Setup 2. Measurement of the diameter of the beam spots and the centre-to-centre distances allowed the divergence of the beam to be determined. The divergence in the x and y directions was determined to be $x' = 1.6\,\mathrm{mrad}$ and $y' = 0.5\,\mathrm{mrad}$, respectively.

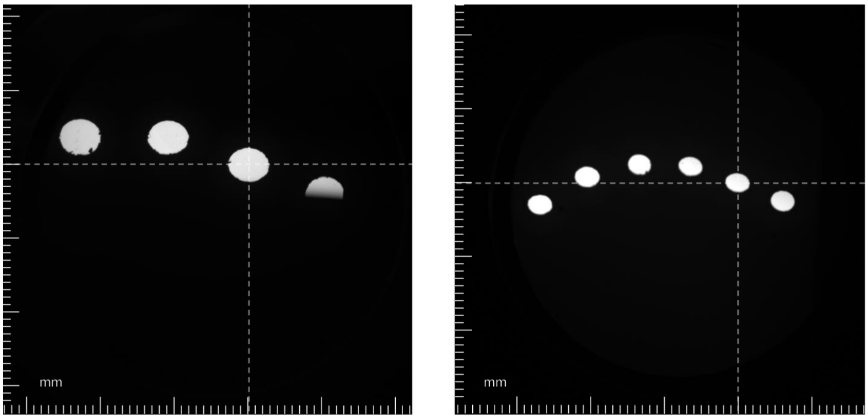

Figure 9. Observed camera image of the three beam spots beyond the aperture in the Setup 1 configuration, left, and with six beam spots beyond the aperture in the Setup 2 configuration, right. Both images were taken with the lens off. The dashed lines indicate the beam axis and the central beam spot.

Images of the beam with the lens operating at a voltage of 20 kV are shown for currents of 28 A and 33 A in Figure 10. The figure shows that the effect of the lens is to produce ring-like structures on the phosphor screen. The diameter and eccentricity of the rings increases with radial distance from the beam axis. The brightness of the image is observed to vary around the ring. This effect is seen more clearly in Figure 11 which shows the intensity distribution plotted as a function of position on the phosphor screen. The ring-like structure of the beam spots is clearly visible against the low background and the non-uniformity of the intensity distribution is also observed. The integrated intensity as well as the intensity distribution around the ring differs from ring to ring. Similar behaviour has previously been reported in [59,60].

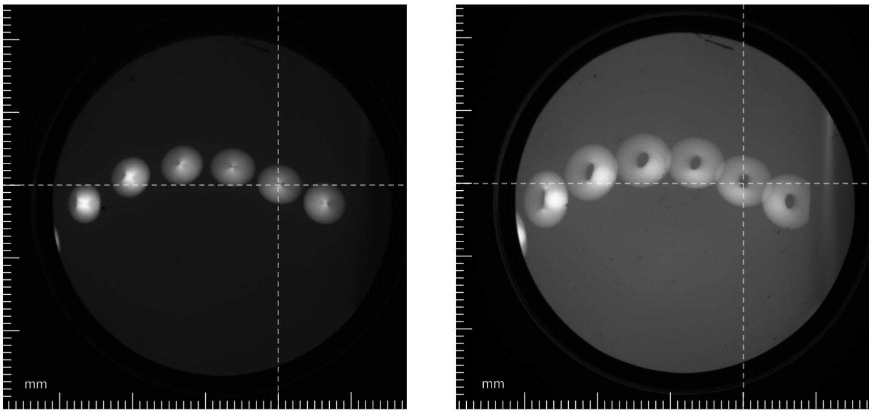

Figure 10. Observed camera image of the six beam spots beyond the aperture in the Setup 2 configuration with the lens on at a current through the coils of 28 A, left and 33 A, right. Both images were taken with a lens voltage of 20 kV. An additional spot is visible on the left hand side, as the lens focusing is increased. The dashed lines indicate the beam axis.

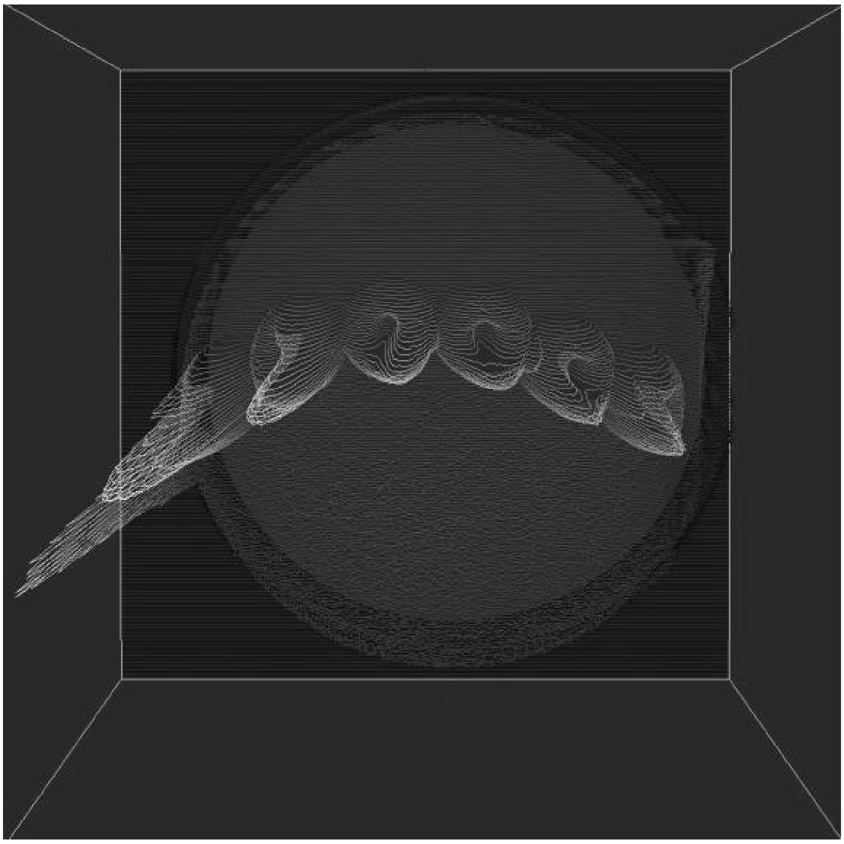

Figure 11. 3D plot of the scintillator measurement of the 6 beam spots in the Setup 2 configuration, with the lens on. The image is shown looking down along the beam axis.

To understand better the distribution of the space charge inside the lens and the plasma dynamics during the beam test, a particle-in-cell (PIC) code VSIM [61] was used to study the main characteristics of a plasma instability that converts pencil beams into rings. The geometry of the central anode, the two end electrodes, and the vacuum tube was reproduced in VSim. A 3D magnetic field map obtained using the actual configuration of the coil was imported from a separate finite-element-analysis package. Thus, the field map described the radially confining magnetic field. The voltage on the central anode was set such that the longitudinal-confinement condition imposed a limit on the maximum electron density which was equal to that imposed by the radial-confinement theory.

The electron cloud was modelled [62] as a collision-less plasma using the particle-in-cell (PIC) method in VSim [61]. The electrostatic potential was calculated from the charge density by solving Poisson's equation on a 3D grid. Then, the macro-particles were advanced in time according to the Lorentz equation. The time step was set to 0.2 ns (corresponding to $\approx 6\tau_c$, where $\tau_c = 2\pi$ m/eB is the cyclotron period) to track the electron movement correctly. The grid had a transverse cell size $\Delta x = 0.14\lambda_D$ and longitudinal cell size $\Delta z = 0.8\lambda_D$, where λ_D is the Debye length. Each macro-particle represented approximately 2000 real electrons.

To drive an instability the electrons were loaded at the beginning of the simulation as a plasma column displaced from the central axis or with a large positive radial gradient in the electron density. The six, 1.4 MeV, proton pencil beams were modelled as macro-particles entering the lens and left to propagate through the electron plasma. The simulation registered the distribution of the proton macro-particles that hit the exit plane of the lens. These macro-particles were then tracked separately through an additional drift space of 67 cm.

The protons were propagated through the electron plasma using VSIM to simulate the impact of a number of plasma instabilities that have been observed experimentally [63,64]:

a hollow electron ring and the diocotron instability [65]. The diocotron modes observed in the simulations corresponded to higher order modes with an azimuthal mode number $m > 1$. Within the range of electron densities between 1×10^{13} m^{-3} and 1×10^{15} m^{-3}, no ring formation was observed in the simulations. The instabilities named above show good azimuthal symmetry during their evolution and, hence, would focus the pencil beams to the same position at all times. A displacement of the bulk of the plasma from the central axis and the rotation of the focusing centre are necessary for the formation of rings. An example of such an instability is shown in Figure 12 and consists of a region of high electron density and a region of low electron density that rotate around the beam axis. Figure 12 shows the result of tracking six proton pencil beams through the instability. Rings are formed on a screen downstream of the lens. In the PIC simulation, the instability was gradually damped due to the absence of a driving mechanism. As the bulk of the plasma approaches the central axis, each pencil beam is focused on a ring with a radius that decreases and a centre that shifts with time. Thus, in the simulation, each pencil beam is transformed into a set of overlapped rings. By contrast, in the experiment, each pencil beam produced a single ring. This experimental outcome was observed consistently throughout the two days of the beam test.

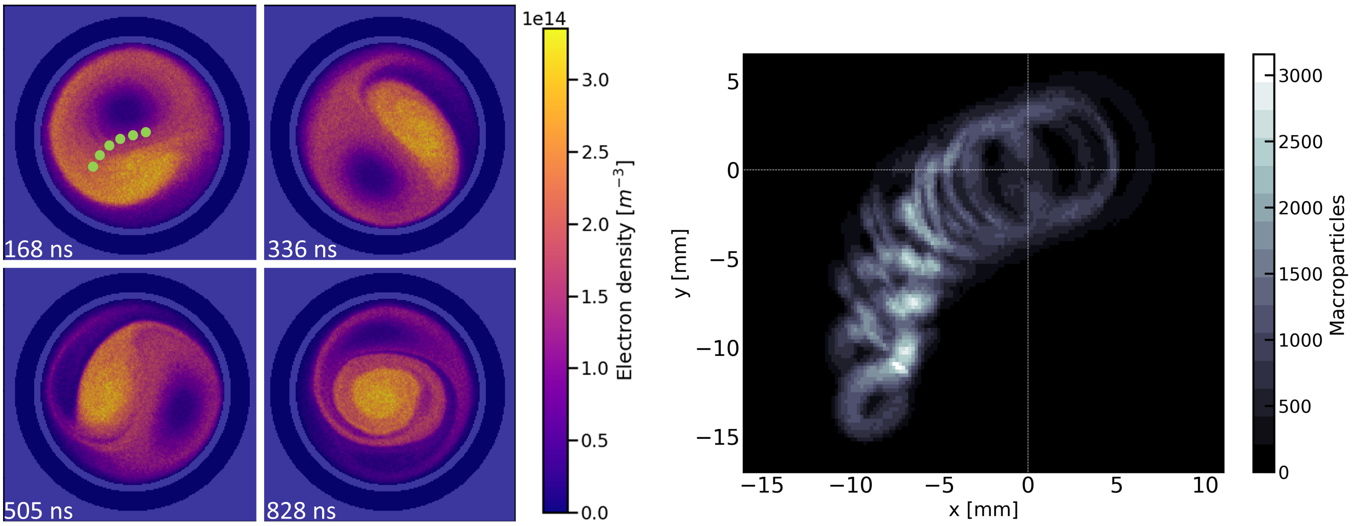

Figure 12. PIC [61] simulation of a plasma instability that was observed to focus the proton pencil beams into rings. **Left**: the averaged density of plasma in a transverse cross-section through the lens at four different time steps during the evolution of the instability. The green spots mark the entry position of the pencil beams. **Right**: number of macroparticles hitting a screen 67 cm downstream of the lens.

A Monte Carlo particle-tracking code, BDSIM [65], was used to simulate the formation of the rings on a screen downstream of the lens for a simplified plasma distribution. The electron cloud was modelled according to the main features of the $m = 1$ diocotron mode, as a longitudinal column of electrons with azimuthal symmetry. The central axis of the column was displaced from the beam axis and rotated around the beam axis with a constant period that was larger than the transit time of the protons through the lens. The electron cloud had a region of constant density in the centre and a negative radial gradient up to the walls of the anode [62]. A 3D time-dependent electric field map was calculated from the rotating plasma column. To study the focusing effect of the plasma and the lens, the six proton pencil beams were tracked through the electric and magnetic field maps. The initial phase-space of the protons upstream of the lens was tuned such that the intensity profile of the pencil beams on the screen obtained from the simulation matches the images taken during the beam test with the lens off.

Figure 13 shows the focusing effect of a rotating plasma column on the pencil beams as a result of the particle tracking. A variation of the separation between the rings and the width of each ring is seen as a function of the density of the plasma. The shape and thickness of the rings are influenced by changes in the electron density and in the radius of rotation of the plasma column. The eccentricity of the rings increases for the pencil beams that are further away from the beam axis as a result of the different focusing strengths in the x and y directions. This geometrical effect depends on the relative position of the pencil beam with respect to the rotation axis of the plasma column. As in the experimental observations, the brightness of each ring is seen to vary along the circumference. The simulations indicated that the position and extent of the intensity peak is dependent on the ratio between the period of rotation of the plasma column and the transit time of the protons through the lens.

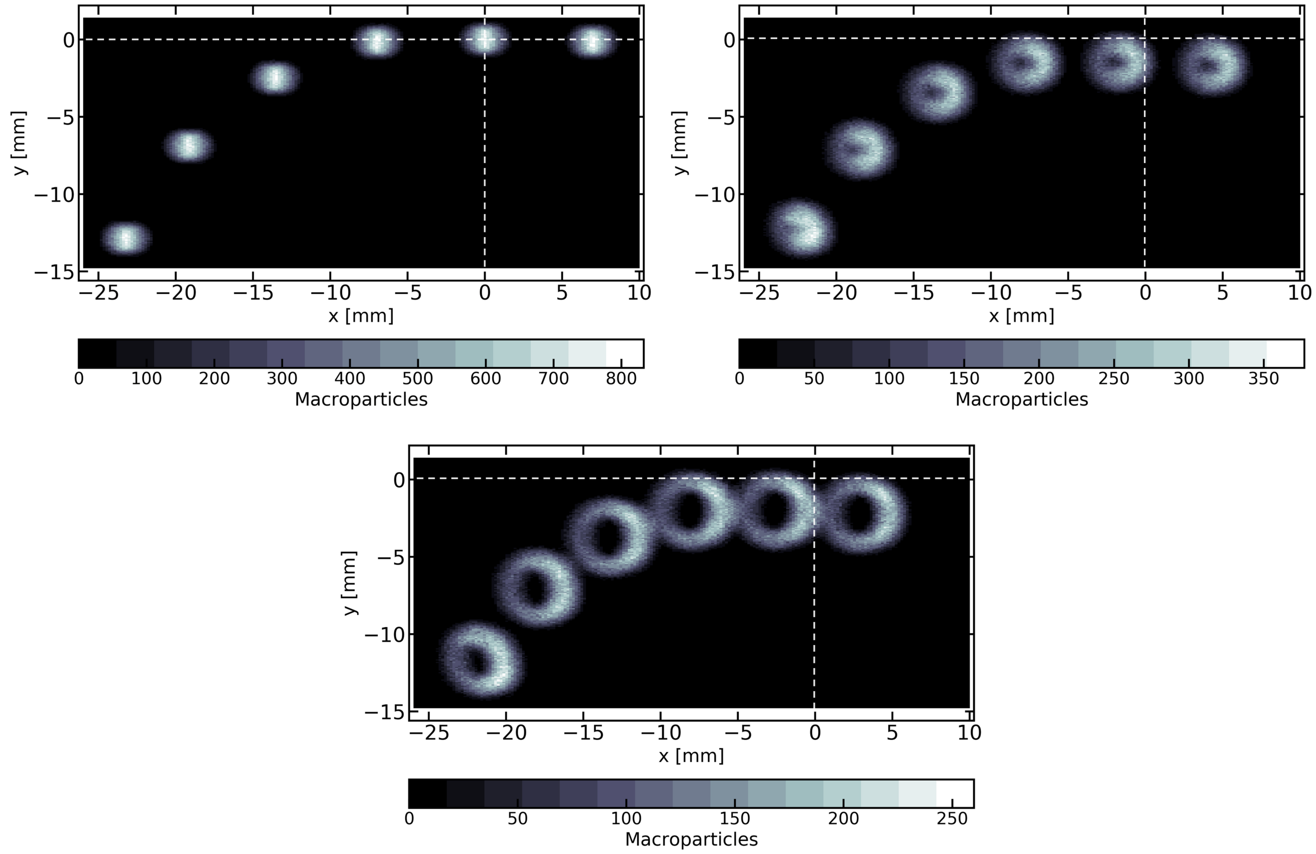

Figure 13. The effect of a plasma column rotating around the beam axis on six proton pencil beams as simulated with BDSIM [65] for electron densities of $0\,\mathrm{m}^{-3}$, $1.8 \times 10^{14}\,\mathrm{m}^{-3}$, and $2.8 \times 10^{14}\,\mathrm{m}^{-3}$. Increasing the density of the plasma modifies the separation and the width of the rings. The plasma column has a radius $\mathrm{r_c} = 14\,\mathrm{mm}$ and an offset $\mathrm{D} = 7\,\mathrm{mm}$ from the central axis of the lens.

A systematic study of the characteristics of the rings was carried out as a function of the voltage and current settings at which the lens was operated during the beam test. Three parameters were used to characterise the rings:

1. Centroid $\mathbf{r_c} = (x_c, y_c)$: The centroid was taken to be the weighted average of all the pixels constituting a ring above a fixed intensity threshold $(x_c, y_c) = \left(\frac{M_{10}}{M_{00}}, \frac{M_{01}}{M_{00}}\right)$, where M_{ij} are the image moments $M_{ij} = \sum_x \sum_y x^i y^j I(x,y)$ of the pixel intensity $I(x,y)$.
2. Diameter, $\mathcal{D}_{x,y}$: The diameter of the ring (or of the beam spot in images taken with the lens off) was determined along the x and y directions separately. The diameter is defined as the width of a beam spot or ring along the x or y direction after an intensity cutoff was applied to a camera image.

3. Eccentricity, $\mathcal{E}$: The eccentricity is defined as the ratio $\frac{\mathcal{D}_x}{\mathcal{D}_y}$.

In order to extract the diameter and the position of the centroid of each ring, an intensity cutoff was applied to the camera images. This procedure introduces an associated uncertainty in the calculations. For the parameters given above, the uncertainties are ± 0.3 mm for $\mathcal{D}_x$, ± 0.2 mm for $\mathcal{D}_y$, and ± 0.05 mm for x_c and y_c.

A comparison of the effects of electric field only and magnetic field only in the lens is shown in Figure 14. This plot presents data from Setup 1, in which the 3 spots are those shown in Figure 9, with the rightmost point corresponding to the beam axis. As expected, applying only an electric potential does not influence the particle transport, while a variation in the magnetic field leads to a more significant change in the focusing strength. Comparison between magnetic field only data and the results of particle transport in the magnetic field shows good agreement in direction as well as in magnitude. This is true for all three of the observed pencil beamlets. The small variation around the pencil beam on the beam axis indicates that the beam axis, aperture axis, and lens axis were not identical.

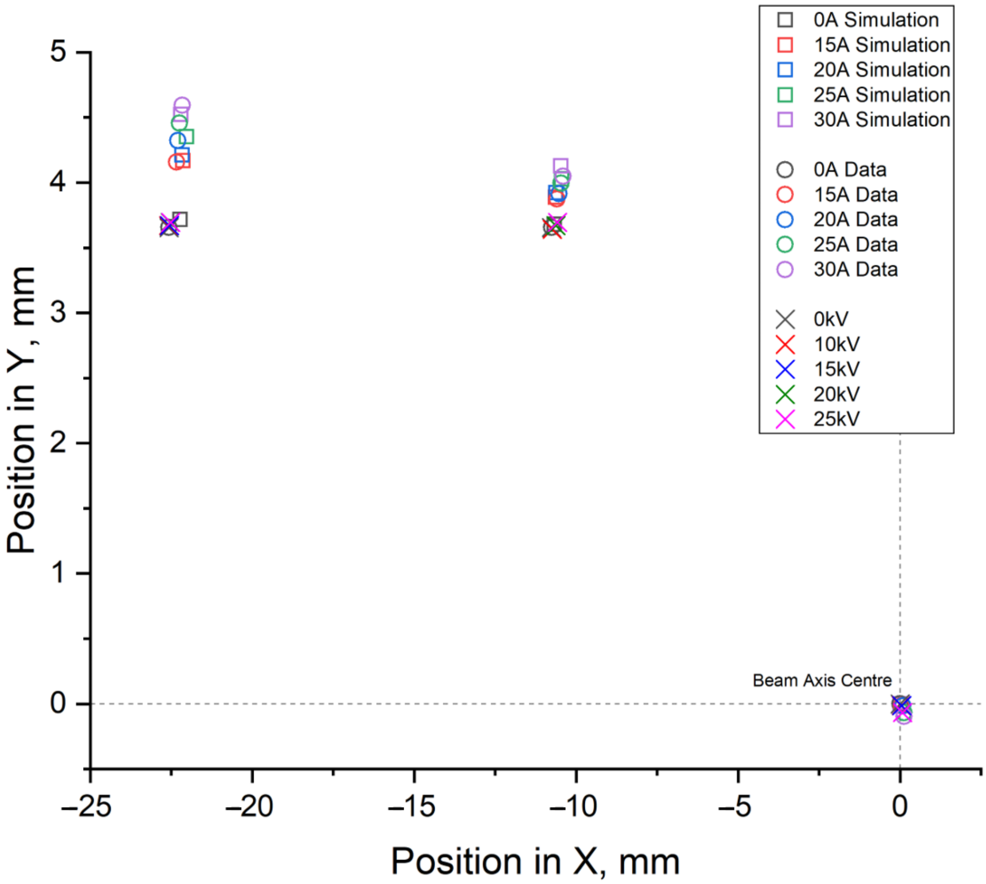

Figure 14. Position of the centroid of the 3 beam spots for varying magnetic fields and high voltages. Squares and Circles represent variation in current through the magnetic coils only, in simulation and data respectively, with no applied high voltage. Crosses represent variation in high voltage (and therefore electric field) with no current through the magnetic coils.

Figure 15 shows the variation in x and y position of the three beam spot centroids in Setup 1, under the effects of both applied magnetic field and high voltage. In this case, the high voltage was held at 15 kV, while the current through the magnetic coils was varied from 0 to 32 A. An approximately linear increase with magnetic field was observed. In addition to the circular motion of the plasma in the lens, there is a focusing force that increased with the external magnetic field. A possible cause for this effect is a misalignment between the beam axis and the symmetry axis of the coil. The two sets of data, for 15 kV and 20 kV, were taken on consecutive days which indicated that the driving mechanism associated with the observed plasma dynamics was a characteristic of the geometry and operation of the lens.

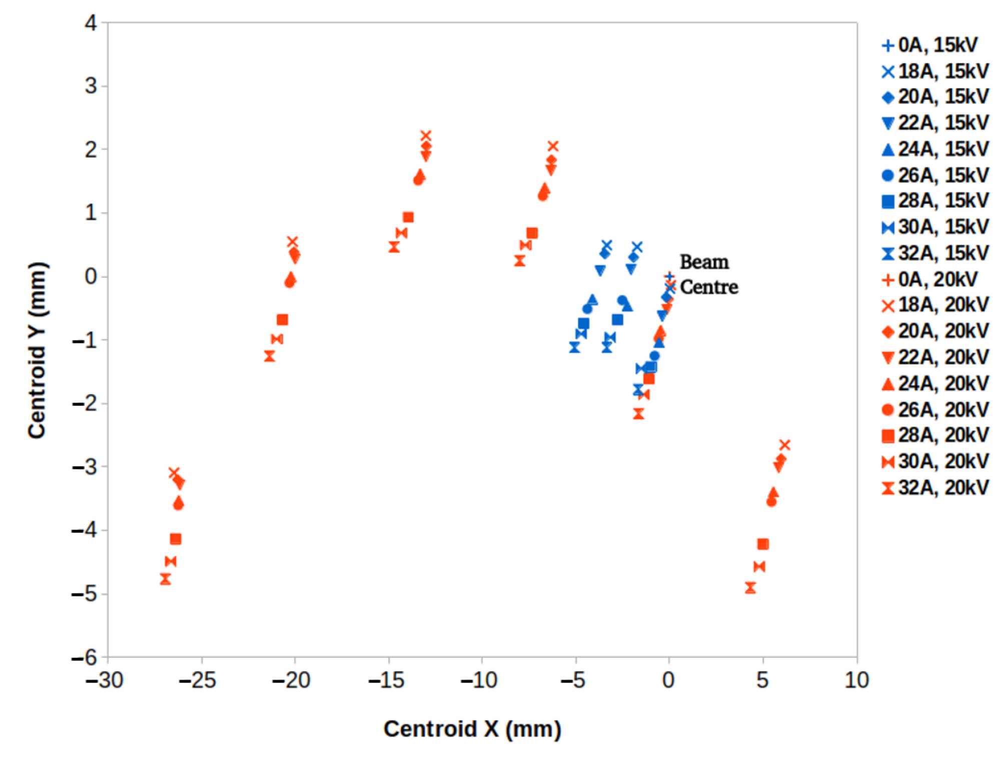

Figure 15. The x and y position of the centroids of the beam spots imaged with the Setup 1 (blue) and Setup 2 (red) with increasing magnetic field strength.

The variation in x and y diameter of the six beam spots from Setup 2 is given in Figure 16: with a constant applied voltage of 15 kV, the variation in spot diameter with magnetic field is shown. A non-linear increase in spot size with change in magnetic fields was observed, with the rate of increase in diameter getting larger at high magnetic fields. This indicated that the increase in plasma density with magnetic field was faster than linear and thus that the plasma trapping efficiency varied with the magnetic field strength. Since the points remained within the lines shown, there was an indication of a trend for the change in diameter for a given spot. The ratio variation being solely dependent on initial position of the spot indicates that this effect is caused by the density distribution of the plasma in the transverse plane.

Figure 17 shows the change in xy ratio of the six beam spots from Setup 2 with variation in magnetic field. The focusing force in the x direction compared to the focusing force in the y direction changed differently for each beam spot. The difference between the two focusing forces was more significant for those beam spots at greater distances from the beam axis. This indicated that the centre of the lens has a low plasma density, while further from the axis of the lens, the plasma density increased with radius. In addition, there was some perturbation that caused the motion of the plasma to evolve with time. Figures 14–17 may be understood in terms of a position dependent plasma density, with the bulk of the plasma shifted radially from the lens centre and rotating around the central axis.

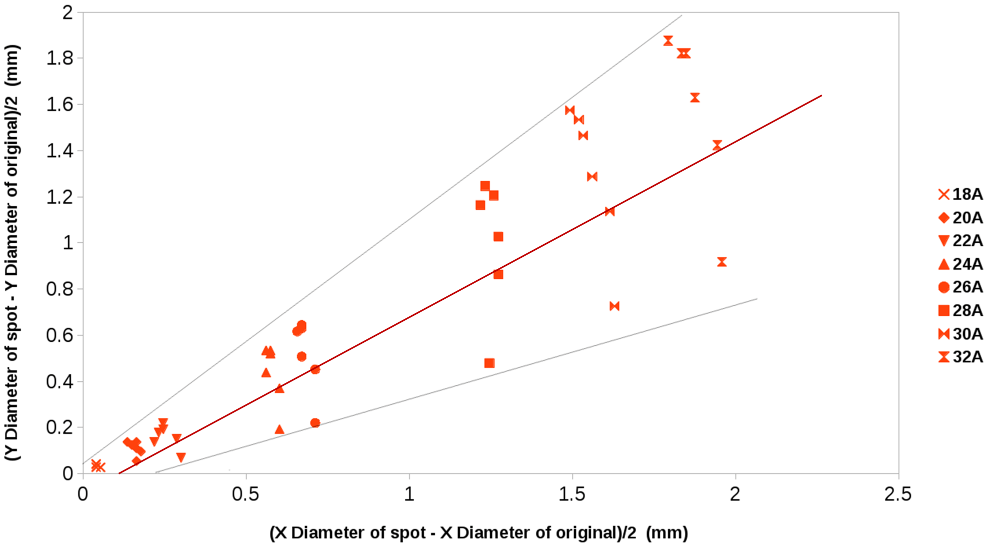

Figure 16. The variation in the x and y diameter of the six spot data with increasing magnetic field strength.

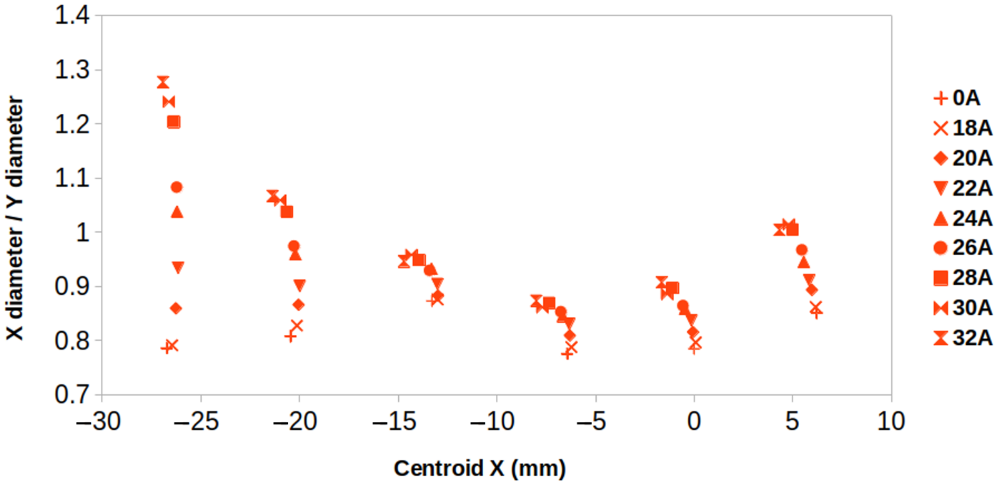

Figure 17. The ratio of the x diameter to the y diameter for beam spots in the six spot data with increasing magnetic field strength.

6. Conclusions

We characterised the operation of an electron plasma (Gabor) lens based on a test at the Surrey Proton Beam Centre with a 1.4 MeV proton beam. Prior measurements at Imperial College indicated that the lens had a stable regime of operation over a range of applied voltage and current. During the beam test, the lens was observed to transform pencil beams into rings. The presence of a plasma was confirmed by matching the measured focusing effect with particle transport calculations. An evaluation of the focusing strength showed that the density of the trapped electrons depends on the strength of the radially confining magnetic field, effects that were well described by simulation. Since the same focusing effects and ring patterns were observed on consecutive days, the plasma instability was associated with the geometry and operation of the lens.

The formation of rings indicates that the plasma column is excited into a coherent off-axis rotation. The size of the rings increases with increasing current through the coil. A reproducible modulation of the intensity was observed around the circumference of each ring. The position of the centroids of the rings varied non-linearly with the external magnetic field strength, showing a variable plasma trapping efficiency. The x and y diameters, and the eccentricity of the rings were seen to depend on their position with respect to the beam axis, as a result of the different x and y focusing forces experienced by each pencil beam.

Both particle-in-cell and particle-tracking simulations showed that a rotation of the bulk of the plasma transforms pencil beams into rings. The size and width of the rings were shown to be determined by the density of the plasma. Rings with size, eccentricity, and intensity modulation similar to the experimental images were reproduced with a simulation of particle transport through a plasma characterised by the $m = 1$ diocotron instability.

The results described here indicate the presence of a mechanism that drives the rotation of the plasma column. Further investigations are required to identify and describe the exact mechanism that needs to be avoided for the lens to be operated as a reliable focusing device.

Author Contributions: Conceptualization, T.N., T.S.-D., R.B., H.-T.L., K.L., J.P. and C.W.; data curation, T.N., T.-S.D., C.L.C. and J.P.; formal analysis, T.N., T.-S.D., C.L.C. and J.P.; funding acquisition, K.L. and J.P.; investigation, T.N., T.-S.D., R.B., C.L.C., H.-T.L., K.L., J.P. and C.W.; methodology, T.N., T.-S.D., K.L. and J.P.; project administration, K.L. and J.P.; resources, K.L. and J.P.; software, T.N., T.-S.D., C.L.C., H.-T.L. and J.P.; supervision, K.L. and J.P.; validation, T.N., T.-S.D. and J.P.; visualization, T.N., T.-S.D. and C.L.C.; writing—original draft, T.N., T.-S.D., K.L. and J.P.; writing—review & editing, T.N., T.-S.D., R.B., H.-T.L., K.L. and C.W. All authors have read and agreed to the published version of the manuscript.

Funding: This research was funded by the STFC through the Imperial Impact Acceleration Account.

Institutional Review Board Statement: Not applicable.

Informed Consent Statement: Not applicable.

Data Availability Statement: The data presented in this study are openly available in FigShare at [10.6084/m9.figshare.14566485].

Acknowledgments: We wish to acknowledge the work of Piero Posocco at the 2017 beam test. We would also like to the thank all the staff at the University of Surrey Ion Beam Facility, and in particular Vladimir Palitsin, for his support throughout both days of the beam test. We gratefully acknowledge the Plasma Physics Group at Imperial College London who were generous in sharing their scientific insight and provided technical support at various stages of the project. The work was financially supported by the STFC through the Imperial Impact Acceleration Account. One of us (TSD) gratefully acknowledges the support from the Class of 1964 Scholarship.

Conflicts of Interest: The authors declare no conflict of interest.

References

1. Moehs, D.P.; Peters, J.; Sherman, J. Negative hydrogen ion sources for accelerators. *IEEE Trans. Plasma Sci.* **2005**, *33*, 1786–1798. [CrossRef]
2. Lawrie, S. Understanding the Plasma and Improving Extraction of the ISIS Penning H-ions Source. Ph.D. Thesis, University of Oxford, Oxford University Research Archive (ORA), Bodleian Libraries, Osney One, Osney Mead, Oxford, UK, 2017.
3. Faircloth, D.; Lawrie, S. An overview of negative hydrogen ion sources for accelerators. *New J. Phys.* **2018**, *20*, 25007. [CrossRef]
4. Tinschert, K.; Iannucci, R.; Lang, R. Electron cyclotron resonance ion sources in use for heavy ion cancer therapy. *Rev. Sci. Instrum.* **2008**, *79*, 02C505. [CrossRef] [PubMed]
5. Kitagawa, A.; Fujita, T.; Muramatsu, M.; Biri, S.; Drentje, A.G. Review on heavy ion radiotherapy facilities and related ion sources (invited). *Rev. Sci. Instrum.* **2010**, *81*, 02B909. [CrossRef]
6. Chao, A.W.; Mess, K.H.; Tigner, M.; Zimmermann, F. *Handbook of Accelerator Physics and Engineering*, 2nd ed.; World Scientific: Singapore, 2013; Chapter Subsystems, pp. 543–765. [CrossRef]
7. Nishiuchi, M.; Daito, I.; Ikegami, M.; Daido, H.; Mori, M.; Orimo, S.; Ogura, K.; Sagisaka, A.; Yogo, A.; Pirozhkov, A.S.; et al. Focusing and spectral enhancement of a repetition-rated, laser-driven, divergent multi-MeV proton beam using permanent quadrupole magnets. *Appl. Phys. Lett.* **2009**, *94*, 061107. [CrossRef]
8. Busold, S.; Schumacher, D.; Deppert, O.; Brabetz, C.; Kroll, F.; Blažević, A.; Bagnoud, V.; Roth, M. Commissioning of a compact laser-based proton beam line for high intensity bunches around 10 MeV. *Phys. Rev. ST Accel. Beams* **2014**, *17*, 031302. [CrossRef]
9. Bulanov, S.V.; Esirkepov, T.; Khoroshkov, V.S.; Kuznetsov, A.V.; Pegoraro, F. Oncological hadrontherapy with laser ion accelerators. *Phys. Lett. Sect. Gen. At. Solid State Phys.* **2002**, *299*, 240–247. [CrossRef]
10. Malka, V.; Fritzler, S.; Lefebvre, E.; d'Humières, E.; Ferrand, R.; Grillon, G.; Albaret, C.; Meyroneinc, S.; Chambaret, J.P.; Antonetti, A.; et al. Practicability of protontherapy using compact laser systems. *Med. Phys.* **2004**, *31*, 1587–1592. [CrossRef] [PubMed]

11. Daido, H.; Nishiuchi, M.; Pirozhkov, A.S. Review of laser-driven ion sources and their applications. *Rep. Prog. Phys.* **2012**, *75*, 56401. [CrossRef] [PubMed]
12. Bin, J.; Allinger, K.; Assmann, W.; Dollinger, G.; Drexler, G.A.; Friedl, A.A.; Habs, D.; Hilz, P.; Hoerlein, R.; Humble, N.; et al. A laser-driven nanosecond proton source for radiobiological studies. *Appl. Phys. Lett.* **2012**, *101*, 243701. [CrossRef]
13. Pozimski, J.; Aslaninejad, M. Gabor lenses for capture and energy selection of laser driven ion beams in cancer treatment. *Laser Part. Beams* **2013**, *31*, 723–733. [CrossRef]
14. Pozimski, J.; Aslaninejad, M.; Posocco, P.A. Advanced Gabor Lens Lattice for Laser Driven Hadron Therapy and Other Applications. In Proceedings of the 7th International Particle Accelerator Conference, Busan, Korea, 8–13 May 2016. [CrossRef]
15. Romano, F.; Schillaci, F.; Cirrone, G.A.P.; Cuttone, G.; Scuderi, V.; Allegra, L.; Amato, A.; Amico, A.; Candiano, G.; De Luca, G.; et al. The ELIMED transport and dosimetry beamline for laser-driven ion beams. *Nucl. Instrum. Methods Phys. Res. Sect. Accel. Spectrometers Detect. Assoc. Equip.* **2016**, *829*, 153–158. [CrossRef]
16. Aymar, G.; Becker, T.; Boogert, S.; Borghesi, M.; Bingham, R.; Brenner, C.; Xiao, R. The Laser-hybrid Accelerator for Radiobiological Applications. *Front. Phys.* **2020**, *8*, 567738. [CrossRef]
17. Zeil, K.; Kraft, S.D.; Bock, S.; Bussmann, M.; Cowan, T.E.; Kluge, T.; Metzkes, J.; Richter, T.; Sauerbrey, R.; Schramm, U. The scaling of proton energies in ultrashort pulse laser plasma acceleration. *New J. Phys.* **2010**, *12*, 45015. [CrossRef]
18. Prasad, R.; Andreev, A.A.; Ter-Avetisyan, S.; Doria, D.; Quinn, K.E.; Romagnani, L.; Brenner, C.M.; Carroll, D.C.; Dover, N.P.; Neely, D.; et al. Fast ion acceleration from thin foils irradiated by ultra-high intensity, ultra-high contrast laser pulses. *Appl. Phys. Lett.* **2011**, *99*, 121504, [CrossRef]
19. Green, J.S.; Robinson, A.P.L.; Booth, N.; Carroll, D.C.; Dance, R.J.; Gray, R.J.; MacLellan, D.A.; McKenna, P.; Murphy, C.D.; Rusby, D.; et al. High efficiency proton beam generation through target thickness control in femtosecond laser-plasma interactions. *Appl. Phys. Lett.* **2014**, *104*, 214101. [CrossRef]
20. Dover, N.; Nishiuchi, M.; Sakaki, H.; Kondo, K.; Lowe, H.; Alkhimova, M.; Ditter, E.; Ettlinger, O.; Faenov, A.; Hata, M.; et al. Demonstration of repetitive energetic proton generation by ultra-intense laser interaction with a tape target. *High Energy Density Phys.* **2020**, *37*, 100847. [CrossRef]
21. Margarone, D.; Velyhan, A.; Dostal, J.; Ullschmied, J.; Perin, J.P.; Chatain, D.; Garcia, S.; Bonnay, P.; Pisarczyk, T.; Dudzak, R.; et al. Proton Acceleration Driven by a Nanosecond Laser from a Cryogenic Thin Solid-Hydrogen Ribbon. *Phys. Rev. X* **2016**, *6*, 041030. [CrossRef]
22. Morrison, J.T.; Feister, S.; Frische, K.D.; Austin, D.R.; Ngirmang, G.K.; Murphy, N.R.; Orban, C.; Chowdhury, E.A.; Roquemore, W.M. MeV proton acceleration at kHz repetition rate from ultra-intense laser liquid interaction. *New J. Phys.* **2018**, *20*, 22001. [CrossRef]
23. Schreiber, J.; Bell, F.; Grüner, F.; Schramm, U.; Geissler, M.; Schnürer, M.; Ter-Avetisyan, S.; Hegelich, B.M.; Cobble, J.; Brambrink, E.; et al. Analytical Model for Ion Acceleration by High-Intensity Laser Pulses. *Phys. Rev. Lett.* **2006**, *97*, 045005. [CrossRef] [PubMed]
24. Qiao, B.; Zepf, M.; Borghesi, M.; Geissler, M. Stable GeV Ion-Beam Acceleration from Thin Foils by Circularly Polarized Laser Pulses. *Phys. Rev. Lett.* **2009**, *102*, 145002. [CrossRef]
25. Roth, M.; Cowan, T.E.; Key, M.H.; Hatchett, S.P.; Brown, C.; Fountain, W.; Johnson, J.; Pennington, D.M.; Snavely, R.A.; Wilks, S.C.; et al. Fast Ignition by Intense Laser-Accelerated Proton Beams. *Phys. Rev. Lett.* **2001**, *86*, 436–439. [CrossRef]
26. Shmatov, M.L. Some problems related to heating the compressed thermonuclear fuel through the cone. *Fusion Sci. Technol.* **2003**, *43*, 456–467. [CrossRef]
27. Gabor, D. A space-charge lens for the focusing of ion beams. *Nature* **1947**, *160*, 89. [CrossRef] [PubMed]
28. Mobley, R.; Gamml, G.; Maschke, A. *Gabor Lenses*; Report BNL–25787; Brookhaven National Lab.: Upton, NY, USA, 1979.
29. Lefevre, H.W.; Booth, R. Progress in Space Charge Lens Development. *IEEE Trans. Nucl. Sci.* **1979**, *26*, 3115–3117. [CrossRef]
30. Palkovic, J.A.; Hren, R.; Lee, G.; Mills, F.E.; Schmidt, C.W.; Wendt, J.; Young, D.E. Measurements on a Gabor Lens for Neutralizing and Focusing a 30-KeV Proton Beam. In Proceedings of the 1988 Linear Accelerator Conference (LINAC 88), Newport News, VA, USA, 3–7 October 1988.
31. Tauschwitz, A.; Boggasch, E.; Wetzler, H.; Hoffmann, D.H.H.; Neuner, U.; Stetter, M.; Stöwe, S.; Tkotz, R.; de Magistris, M.; Seelig, W. Plasma lens focusing of heavy ion beams utilizing a wall-stabilized discharge. In Proceedings of the 1994 10th International Conference on High-Power Particle Beams, San Diego, CA, USA, 20–24 June 1994; Volume 2, pp. 695–698.
32. Chekh, Y.M.; Goncharov, A.A.; Protsenko, I.M.; Dobrovolsky, A.M.; Brown, I.G. Electrostatic plasma lens for accelerator injection application. *Rev. Sci. Instrum.* **2006**, *77*, 03B906, [CrossRef]
33. Dobrovolskiy, A.; Dunets, S.; Evsyukov, A.; Goncharov, A.; Gushenets, V.; Litovko, I.; Oks, E. Recent advances in plasma devices based on plasma lens configuration for manipulating high-current heavy ion beams. *Rev. Sci. Instrum.* **2010**, *81*, 02B704, [CrossRef]
34. Schulte, K.; Droba, M.; Meusel, O.; Ratzinger, U.; Adonin, A.; Berezov, R.; Hollinger, R.; Pfister, J. Gabor Lens Performance Studies at the GSI High Current Test Injector. In Proceedings of the 4th International Particle Accelerator Conference (IPAC 2013), Shanghai, China, 12–17 May 2013; p. THPWO021.
35. Pozimski, J.; Meusel, O. Space charge lenses for particle beams. *Rev. Sci. Instrum.* **2005**, *76*, 063308. [CrossRef]
36. Malmberg, J.H.; de Grassie, J.S. Properties of Nonneutral Plasma. *Phys. Rev. Lett.* **1975**, *35*, 577–580. [CrossRef]
37. Malmberg, J.H.; Driscoll, C.F. Long-Time Containment of a Pure Electron Plasma. *Phys. Rev. Lett.* **1980**, *44*, 654–657. [CrossRef]

38. Pozimski, J.; Gross, P.; Dolling, R.; Weis, T. First experimental studies of a Gabor plasma lens in Frankfurt. *Conf. Proc. C* **1992**, *920324*, 1536–1538.
39. Chekh, Y.; Goncharov, A.; Protsenko, I.; Brown, I.G. Effect of the electrostatic plasma lens on the emittance of a high-current heavy ion beam. *Appl. Phys. Lett.* **2005**, *86*, 041502, [CrossRef]
40. Meusel, O.; Droba, M.; Glaeser, B.; Schulte, K. Experimental studies of stable confined electron clouds using Gabor lenses. *AIP Conf. Proc. C* **2013**, *1206051*, 157–160. [CrossRef]
41. Levy, R.H. Diocotron Instability in a Cylindrical Geometry. *Phys. Fluids* **1965**, *8*, 1288–1295. [CrossRef]
42. Sjobak, K.; Adli, E.; Bergamaschi, M.; Burger, S.; Corsini, R.; Curcio, A.; Curt, S.; Döbert, S.; Farabolini, W.; Gamba, D.; et al. Status of the CLEAR electron beam user facility at CERN. In Proceedings of the 10th International Particle Accelerator Conference (IPAC2019), Melbourne, Australia, 19–24 May 2019.
43. Lindstrøm, C.A.; Adli, E.; Boyle, G.; Corsini, R.; Dyson, A.; Farabolini, W.; Hooker, S.; Meisel, M.; Osterhoff, J.; Röckemann, J.H.; et al. Emittance preservation in an aberration-free active plasma lens. *Phys. Rev. Lett.* **2018**, *121*, 194801. [CrossRef] [PubMed]
44. Lindstrøm, C.A.; Sjobak, K.; Adli, E.; Röckemann, J.H.; Schaper, L.; Osterhoff, J.; Dyson, A.; Hooker, S.; Farabolini, W.; Gamba, D.; et al. Overview of the CLEAR plasma lens experiment. *Nucl. Instrum. Methods Phys. Res. Sect. A* **2018**, *909*, 379–382. [CrossRef]
45. Joshi, C.; Blue, B.; Clayton, C.; Dodd, E.; Huang, C.; Marsh, K.; Mori, W.; Wang, S.; Hogan, M.; O'Connell, C.; et al. High energy density plasma science with an ultrarelativistic electron beam. *Phys. Plasmas* **2002**, *9*, 1845–1855.
46. Hogan, M.J.; Clayton, C.E.; Huang, C.; Muggli, P.; Wang, S.; Blue, B.E.; Walz, D.; Marsh, K.A.; O'Connell, C.L.; Lee, S.; et al. Ultrarelativistic-Positron-Beam Transport through Meter-Scale Plasmas. *Phys. Rev. Lett.* **2003**, *90*, 205002. [CrossRef]
47. Muggli, P.; Blue, B.; Clayton, C.; Decker, F.; Hogan, M.; Huang, C.; Joshi, C.; Katsouleas, T.C.; Lu, W.; Mori, W.; et al. Halo formation and emittance growth of positron beams in plasmas. *Phys. Rev. Lett.* **2008**, *101*, 055001. [CrossRef]
48. Van Tilborg, J.; Steinke, S.; Geddes, C.G.R.; Matlis, N.H.; Shaw, B.H.; Gonsalves, A.J.; Huijts, J.V.; Nakamura, K.; Daniels, J.; Schroeder, C.B.; et al. Active Plasma Lensing for Relativistic Laser-Plasma-Accelerated Electron Beams. *Phys. Rev. Lett.* **2015**, *115*, 184802. [CrossRef]
49. Van Tilborg, J.; Barber, S.K.; Tsai, H.E.; Swanson, K.K.; Steinke, S.; Geddes, C.G.R.; Gonsalves, A.J.; Schroeder, C.B.; Esarey, E.; Bulanov, S.S.; et al. Nonuniform discharge currents in active plasma lenses. *Phys. Rev. Accel. Beams* **2017**, *20*, 032803. [CrossRef]
50. Doss, C.E.; Adli, E.; Ariniello, R.; Cary, J.; Corde, S.; Hidding, B.; Hogan, M.J.; Hunt-Stone, K.; Joshi, C.; Marsh, K.A.; et al. Laser-ionized, beam-driven, underdense, passive thin plasma lens. *Phys. Rev. Accel. Beams* **2019**, *22*, 111001. [CrossRef]
51. Barov, N.; Conde, M.E.; Gai, W.; Rosenzweig, J.B. Propagation of Short Electron Pulses in a Plasma Channel. *Phys. Rev. Lett.* **1998**, *80*, 81–84. [CrossRef]
52. Pompili, R.; Anania, M.P.; Bellaveglia, M.; Biagioni, A.; Bini, S.; Bisesto, F.; Brentegani, E.; Castorina, G.; Chiadroni, E.; Cianchi, A.; et al. Experimental characterization of active plasma lensing for electron beams. *Appl. Phys. Lett.* **2017**, *110*, 104101, [CrossRef]
53. Chiadroni, E.; Anania, M.P.; Bellaveglia, M.; Biagioni, A.; Bisesto, F.; Brentegani, E.; Zigler, A. Overview of Plasma Lens Experiments and Recent Results at SPARC_LAB. *Nucl. Instrum. Meth. A* **2018**, *909*, 16–20. [CrossRef]
54. Pompili, R.; Chiadroni, E.; Cianchi, A.; Del Dotto, A.; Faillace, L.; Ferrario, M.; Iovine, P.; Masullo, M.R. Plasma lens-based beam extraction and removal system for Plasma Wakefield Acceleration experiments. *Phys. Rev. Accel. Beams* **2019**, *22*, 121302, [CrossRef]
55. Dotto, A.D.; Chiadroni, E.; Cianchi, A.; Faillace, L.; Ferrario, M.; Iovine, P.; Masullo, M.; Pompili, R. Compact and tunable active-plasma lens system for witness extraction and driver removal. *J. Phys. Conf. Ser.* **2020**, *1596*, 012050. [CrossRef]
56. Danielson, J.R.; Weber, T.R.; Surko, C.M. Plasma manipulation techniques for positron storage in a multicell trap. *Phys. Plasmas* **2006**, *13*, 123502, [CrossRef]
57. Hurst, N.C.; Danielson, J.R.; Baker, C.J.; Surko, C.M. Confinement and manipulation of electron plasmas in a multicell trap. *Phys. Plasmas* **2019**, *26*, 013513, [CrossRef]
58. University of Surrey Ion Beam Centre. Available online: https://www.surrey.ac.uk/ion-beam-centre (accessed on 19 January 2021).
59. Neuner, U.; Bock, R.; Roth, M.; Spiller, P.; Constantin, C.; Funk, U.N.; Geissel, M.; Hakuli, S.; Hoffmann, D.H.H.; Jacoby, J.; et al. Shaping of Intense Ion Beams into Hollow Cylindrical Form. *Phys. Rev. Lett.* **2000**, *85*, 4518–4521. [CrossRef]
60. Posocco, P.A.; Merchant, M.; Pozimski, J.; Xia, Y. First Test of The Imperial College Gabor (Plasma) Lens prototype at the Surrey Ion Beam centre. In Proceedings of the 7th International Particle Accelerator Conference (IPAC 2016), Busan, Korea, 8–13 May 2016; p. TUPMY024. [CrossRef]
61. VSim for Plasma. 2020. Available online: https://www.txcorp.com/vsim (accessed on 12 April 2021).
62. Dascalu, T.S. *Numerical Study of the First Gabor Lens Prototype*; Technical Note CCAP-TN-ACCL-05; The Centre for the Clinical Application of Particles (CCAP), Imperial College London: London, UK, 2021.
63. Kapetanakos, C.A.; Hammer, D.A.; Striffler, C.D.; Davidson, R.C. Destructive Instabilities in Hollow Intense Relativistic Electron Beams. *Phys. Rev. Lett.* **1973**, *30*, 1303–1306. [CrossRef]
64. Rosenthal, G.; Dimonte, G.; Wong, A.Y. Stabilization of the diocotron instability in an annular plasma. *Phys. Fluids* **1987**, *30*, 3257–3261. [CrossRef]
65. Nevay, L.J.; Boogert, S.T.; Snuverink, J.; Abramov, A.; Deacon, L.C.; Garcia-Morales, H.; Walker, S.D. BDSIM: An accelerator tracking code with particle-matter interactions. *Comput. Phys. Commun.* **2020**, *252*, 107200. [CrossRef]